Widespread intensified pycnocline turbulence in the summer stratified Yellow Sea

Wei Yang,[1] Hao Wei,[1] Zhiyu Liu,[2] Liang Zhao,[3]

[1]School of Marine Science and Technology, Tianjin University, Tianjin, China

[2]State Key Laboratory of Marine Environmental Science, and Department of Physical Oceanography, College of Ocean and Earth Sciences, Xiamen University, Xiamen, China

[3]College of Marine and Environmental Sciences, Tianjin University of Science and Technology, TEDA, Tianjin, China

Corresponding author: Wei Yang, wei_yang@tju.edu.cn

Key points:

- Microstructure measurements suggest widespread intensified pycnocline turbulence in the summer stratified Yellow Sea.
- The observed strong turbulence generally occurs at the upper boundary of a low-salinity water layer where is favorable for salt fingering.
- Potential influences of salt fingering, shear instability, and thermohaline-shear instability on the pycnocline turbulence are discussed.

This article has been accepted for publication and undergone full peer review but has not been through the copyediting, typesetting, pagination and proofreading process, which may lead to differences between this version and the Version of Record. Please cite this article as doi: 10.1029/2022JC019023.

Abstract

Pycnocline mixing lies at the heart of seasonally stratified shelf sea systems, regulating vertical exchange of momentum, mass, heat, and biogeochemical constituents. Based on microstructure measurements in the summer of 2013 and 2017, here we report on the widespread occurrence of intensified pycnocline turbulence in the summer stratified Yellow Sea (YS). Large turbulent kinetic energy dissipation rates $\varepsilon \sim \mathcal{O}$ (10^{-7} W kg^{-1}) and microscale thermal dissipation rates $\chi \sim \mathcal{O}$ (10^{-6} K^2 s^{-1}) are found in the pycnocline below the depth of the strongest stratification at many sampling stations. Shipboard velocity measurements suggest that wind-induced near-inertial internal waves induced strong velocity shear; however, the calculated velocity shear peaked exactly at (instead of below) the strongest stratification layer and is generally not strong enough to trigger shear instabilities according to the Richardson number criterion. Example results at two repeated sampling stations clearly showed the presence of a low-salinity water layer (with a thickness of 5–15 m), at the upper boundary of which salt fingering is expected to occur according to the Turner angle. The observed elevated ε and χ tended to occur in the salt-finger-favorable layers. Although the distribution of ε and χ reveals the relation with Turner angle, we further note the possible complexity in the driving mechanisms with the thermohaline-shear instability potentially playing a role. Given the widespread nature of the intensified pycnocline turbulence, it is expected that this turbulence has important implications for nutrients cycling and thus the maintenance of primary productivity in the summer stratified YS.

Plain Language Summary

Mixing within and across the pycnocline in seasonally stratified shelf seas controls nutrients supply from depth, laying the foundation for the growth and distribution of primary producers. Therefore, the quantitation of pycnocline mixing and associated driving mechanism in shelf seas has broad biological significance. Here microstructure profiling measurements in the summer stratified Yellow Sea (YS) reveal an interesting phenomenon of widespread intensified pycnocline turbulence. Analysis of velocity measurements suggest the presence of wind-induced near-inertial internal waves which have induced strong velocity shear across the pycnocline. However, these velocity shear seems cannot directly excite the observed pycnocline turbulence. Interestingly enough, we next find that the strong turbulence mostly occurred at the upper interface of a low-salinity water layer where salt fingering is expected (the Turner angle Tu > 45°). The potential influence of double-diffusive convection, shear

instability, and thermohaline-shear instability to the observed intensified turbulence are discussed. In this study, we have revealed, for the first time, the presence of widespread intensified pycnocline turbulence in the YS. The presented results is thought to have important implications for nutrients cycling and the maintenance of primary productivity in the summer stratified YS.

1. Introduction

Turbulent mixing, which acts to redistribute momentum, heat, freshwater, carbon, and other biogeochemical tracers, lies at the heart of many regional and global-scale processes in the ocean (Munk & Wunch, 1998; Simpson & Sharples, 2012). In shelf seas, the ability of ocean physics modeling has been largely limited by the performance of turbulence closure schemes in characterizing pycnocline mixing (Palmer et al., 2013). This has consequently limited the performance of coupled physical-biogeochemical models, as pycnocline mixing is directly relevant to the supplies of nutrients to the euphotic zone that support the growth of phytoplankton (Sharples & Tett, 1994; Rippeth et al., 2009; Williams et al., 2013; Nagai et al., 2019). Revealing unresolved physical processes and mechanisms as well as their impacts on pycnocline mixing is thus central to current shelf sea studies.

One well-known driving mechanism of pycnocline mixing in shelf seas arises from the shear across the pycnocline as induced by different types of internal waves, such as near-inertial internal waves (NIWs; Mackinnon & Gregg, 2003; van der Lee & Umlauf, 2011), internal tides (ITs; Xu et al., 2020), and internal solitary waves (ISWs; Moum et al., 2003; Bourgault et al., 2011; Yang et al., 2020). Once the velocity shear generated by internal waves overcomes the suppressing effect of stratification, it leads to instabilities generating turbulence and thus mixing of various properties (Rippeth et al., 2005; Liu et al., 2009).

Aside of turbulence generated by breaking internal waves, double-diffusive convection can also induce instabilities and thus enhance mixing of various properties (St. Laurent & Schmitt, 1999; Alford et al., 2005). Double-diffusion develops in the ocean, as diffusive convection or salt fingering, when density is stably stratified but unstably stratified in one of its components (mostly temperature or salinity). Salt fingering occurs where warm and salty layers overlie cooler and fresher water. In shelf seas, the occurrence of double diffusion is usually tied to thermohaline intrusions, i.e., spread of water masses of different potential

temperature and salinity along isopycnals (Woods et al., 1986; Ruddick, 1992; Cyr et al., 2011; Hopkins et al., 2012).

Double diffusion utilizes the potential energy of temperature or salinity (depending on which one is unstably stratified) and is usually thought to work slowly as opposed to the more energetic mechanically-driven turbulent mixing (Schmitt, 1994). However, this expectation has been challenged by more and more field observations which revealed intensified turbulence in intrusive layers (Larson & Gregg, 1983; Alford et al., 2005; Inoue et al., 2007; Pérez-Santos et al., 2014; Fine et al., 2022). Recent studies argued that the development of double diffusion in the ocean can be different from the classic prediction which ignores the influence of background velocity shear (Kimura & Smyth, 2011; Smyth & Kimura, 2011; Radko, 2016). Once double diffusion interacts with the background shear, the density field exhibits inversions even for flows that are dynamically stable (Radko, 2016). With observations in the Baltic sea Umlauf et al. (2018) showed that in response to an intermittent intrusion, the time scale of diffusive staircases can be much shorter (hours to days) than its characteristic value for quiescent flow.

This study focuses on the Yellow Sea (YS), which is a seasonally stratified shelf sea located in the Northwest Pacific Ocean (Figure 1). Microstructure measurements in the YS revealed that the effect of the tidally induced turbulence at seabed is limited within the bottom boundary layer (Liu et al., 2009; Wei et al., 2014). In contrast to the well-defined boundary layer turbulence (Liu & Wei, 2007; Lozovatsky et al., 2008), the characteristics and associated driving mechanisms of the pycnocline turbulence in the YS remain elusive. Observations and numerical simulations have shown that the YS hosts different types of internal waves, including ITs, NIWs, and ISWs (Liu et al., 2009; Liu et al., 2019; Song et al., 2021; Yang et al. 2021). Available observations have revealed the impacts of ISWs and ITs on pycnocline turbulence in the YS (Liu et al., 2009; Xu et al., 2020). Based on microstructure measurements, Liu et al. (2009) showed that ISWs can lead to the enhancement of turbulent kinetic energy (TKE) dissipation rate by an order of magnitude. More recently, using microstructure measurements at a local shelf slope in the southern YS, Xu et al. (2020) showed that strong turbulence occurred in the lower pycnocline caused by semidiurnal ITs.

Here we attempt to shed some light on characteristics of pycnocline turbulence and the associated complex driving mechanisms in the summer stratified YS based on an extensive dataset, which includes velocity, stratification, and microstructure observations from two cruises carried out during the summer of 2013 and 2017. We will first show an interesting

phenomenon of widespread intensified pycnocline turbulence which is reported for the first time in the YS. The driving mechanisms of this pycnocline turbulence are then investigated. In addition to wind-induced NIWs, the relation between the intensified pycnocline turbulence and the presence of a low-salinity water layer is highlighted.

This paper is organized as follows. Section 2 describes the observations and data analysis methods. Section 3 shows the temporal and spatial variations of turbulence. The physical backgrounds that may be associated with the intensified pycnocline turbulence are also presented. Section 4 discusses the driving mechanisms of the intensified pycnocline turbulence. The results are summarized in Section 5.

2. Methods

2.1. Field surveys

The data analyzed in this study include measurements from two cruises in the YS carried out during 14–19 July 2013 and 29 August–12 September 2017, respectively (Figure 1). For each cruise, there were a repeated sampling station (Stn. C05 and H08, respectively) lasting ~25 h and several transects for microstructure profiling measurements. The Stn. C05 (~123.5°E, ~35°N, with a mean water depth of 67 m), was about one-degree north of Stn. H08 (~123.5°E, ~36°N, 78 m water depth). During both cruises, our main sampling instrument was a Vertical Microstructure Profiler-250 (VMP-250, Rockland Scientific Inc) equipped with two shear probes (sampled at 512 Hz), one FP07 fast-response thermistor, and one SBE 7 micro-conductivity probe. The microscale velocity shear measured by the shear probes was used to estimate the TKE dissipation rate (ε) using isotropic turbulence assumption (Gregg, 1999; Wolk et al., 2002). The microscale temperature fluctuations measured by FP07 thermistor were used to calculate the dissipation rate of thermal variance (χ).

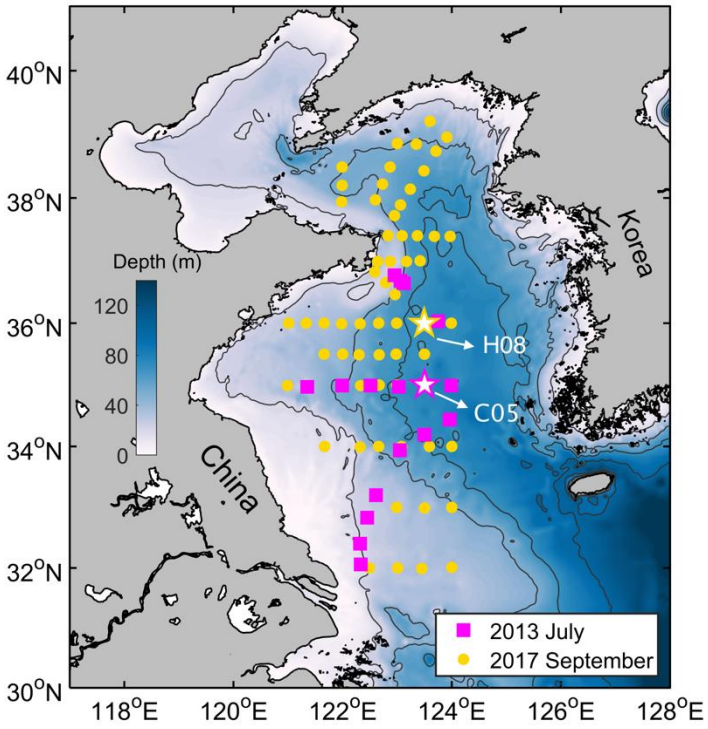

Figure 1. (a) Bathymetry of the Yellow Sea with sampling stations indicated with symbols. The magenta squares and yellow dots indicate the locations of the sampling stations during July 2013 and September 2017, respectively. The magenta and yellow pentagrams indicate the 25-hr repeated sampling stations C05 and H08, respectively.

Standard temperature and salinity data were also collected using a conventional conductivity-temperature-depth (CTD) profiler (RBR620) with a sampling rate of 6 Hz. The RBR620 was deployed once at each station along the transects. To resolve temporal evolutions of the temperature and salinity, RBR620 was deployed once an hour at the two repeated sampling stations. Horizontal velocities, starting from 10 m depth, were continuously measured by a shipboard acoustic Doppler current profiler (ADCP, 300 kHz) only during the cruise in 2017 with vertical and temporal resolutions of 2 m and 2 minutes, respectively.

2.2. Data Processing

The TKE dissipation rate ε was estimated by fitting the empirical Nasmyth spectrum to the measured shear spectra over consecutive segments of 2 m with a 50 % overlap (Figure 2a). As a result, vertical profiles of ε with a vertical resolution of 1 m were obtained (for details of the estimation method we refer to Yang et al., 2020; Xu et al., 2020). With the assumption

of isotropy for small-scale turbulence, χ was calculated from the FP07 thermistor data following

$$\chi = 6\kappa_T \langle (\partial T'/\partial z)^2 \rangle,$$

where κ_T is the molecular thermal diffusivity, $\langle (\partial T'/\partial z)^2 \rangle$ is the variance of the thermal gradient over the same consecutive segments of 2 m with a 50% overlap. To recover the loss of thermal variance at high wavenumbers due to the thermal response limitations, the spectra were corrected using the dynamic response correction function $H^2(f) = \left(1 + \left(\frac{f}{f_c}\right)^2\right)^{-1}$, where $f_c = (2\pi\tau U^{-0.32})^{-1}$ is a speed-dependent cut-off frequency with U being the mean falling speed of VMP and $\tau = 0.005$ s (Gregg & Meagher, 1980; Li & Yamazaki, 2001). The noise spectra were obtained using the noise model given in the ODAS MATLAB Library provided by Rockland Scientific International Inc (black curve in Figure 2b). The noise model was validated by the quiescent segments of our dataset.

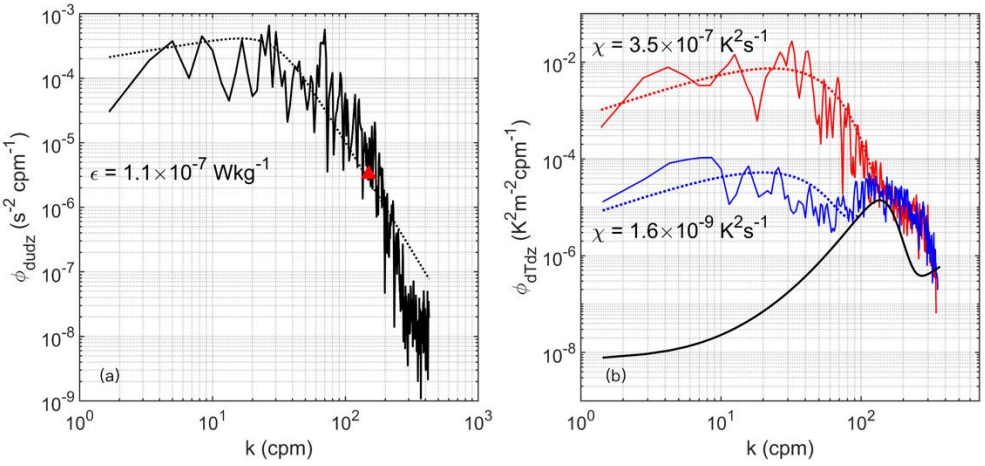

Figure 2. (a) An example of the observed shear spectra (solid line) with the corresponding empirical Nasmyth spectra (dashed line). (b) Examples of the observed temperature gradient spectra (blue and red solid lines) and the corresponding Batchelor spectra (blue and red dashed lines). The modeled noise spectra are also indicated (black line). The end of the two dashed lines represent k_u up to which the fits are made. The calculated χ are texted nearby.

The frequency-response corrected temperature gradient variance spectra were fitted to the theoretical Batchelor spectrum (Batchelor, 1959) using a maximum likelihood estimation (MLE) method, including the rejection criteria (Ruddick et al., 2000). The temperature variance dissipation rate χ was estimated by integrating the temperature gradient spectrum. The upper wavenumber limit that can be integrated depends on both the acceptable correction factor and

the noise spectra. We set a maximum correction factor of 5, corresponding to 30–50 cpm (cycles per meter). Requiring the ratio of the observed to the noise spectra being larger than 2 may change the upper limit further (Sommer et al., 2013; Bluteau et al., 2017). Once χ was determined, maximum likelihood estimation (MLE) was used with the estimated χ to fit the Batchelor spectrum to the observed spectra (Ruddick et al., 2000). Results of two typical segments with the calculated χ having two orders of magnitude difference are shown in Figure 2b. Evidently, the observed spectra agree well with the fitted Batchelor spectra, confirming validity of our estimates of χ.

This spectral estimation, however, has an implicit assumption that the observed thermal gradient is directly related to fully developed isotropic turbulence. This may be violated if there exist sharp temperature interfaces, for example, induced by diffusive steps, lateral intrusions or strong thermocline (instead of turbulence). The associated uncertainty in spectral estimation of χ is analyzed in the appendix of Fine et al. (2018). The summer pycnocline of the YS is characterized by sharp temperature interfaces with vertical gradients of up to 5°C per meter. Following Fine et al. (2018), those segments were first visually identified, and then excluded in the estimation. Missing values were then complimented with interpolation.

To investigate double-diffusive instabilities, we calculated the Turner angle ($Tu = tan^{-1}(\frac{\alpha T_z - \beta S_z}{\alpha T_z + \beta S_z})$), where α and β are coefficients for thermal expansion and saline contraction, and T_z and S_z are the vertical gradients of temperature and salinity, respectively (Ruddick, 1983). The Turner angle is an equivalent parameter of the density ratio ($R_\rho = \frac{\alpha T_z}{\beta S_z}$) but can overcome its large range (Ruddick 1983). Thermohaline structures favorable for salt fingering and diffusive convection have 45° < Tu < 90° and -90° < Tu < -45°, respectively (Ruddick, 1983). Furthermore, the baroclinic velocity ($\boldsymbol{u}'$) was calculated by subtracting the depth-mean velocity ($\boldsymbol{U}$) from the raw velocity ($\boldsymbol{u}$), i.e., $\boldsymbol{u}' = \boldsymbol{u} - \boldsymbol{U}$. The squared velocity shear was calculated following $S^2 = (\frac{\partial u}{\partial z})^2 + (\frac{\partial v}{\partial z})^2$, where u and v are the zonal and meridional velocities, respectively. The squared buoyancy frequency was calculated according to $N^2 = -\frac{g}{\rho_0}\frac{\partial \rho}{\partial z}$, where g is the gravitational acceleration, and ρ is water density. The gradient Richardson number was then calculated according to Ri = $\frac{N^2}{S^2}$.

2.3. The slab mixed-layer model

To investigate wind-induced near-inertial internal waves at the repeated sampling Stn. H08, we conducted a quantitative analysis with the classic slab mixed-layer model (D'Asaro, 1985),

$$\frac{\partial u}{\partial t} - fv = \frac{\tau_x}{\rho H} - ru,$$

$$\frac{\partial v}{\partial t} + fu = \frac{\tau_y}{\rho H} - rv,$$

where H is the mixed layer depth (MLD), r is a damping coefficient parameterizing wave radiation and local dissipation. Here, r was set to be 2 day^{-1} according to the results of Rayson et al. (2015) and Shen et al. (2017) that the shallow water effect damping near-inertial oscillations generally has a time scale of 1–3 inertial periods. The wind stress (τ_x, τ_y) was calculated from the hourly reanalysis ERA5 wind data at the location of Stn. H08 using the Oey et al. (2006) drag coefficient. A constant surface mixed layer depth of 20 m (roughly matching the observation at Stn. H08) was employed.

3. Results

3.1. Temporal variations of turbulence

3.1.1. Station H08

We begin our analysis with temporal variations of turbulence at the two repeated sampling stations. Stn. H08 is occupied by the Yellow Sea Cold Water Mass (YSCWM) at depth which is a basin-scale cold water mass (< 10 °C) underneath the pycnocline in summer. The strongest stratification was located at ~ 23 m as revealed by the squared buoyancy frequency N^2 which shows small vertical displacement (Figure 3c). According to the 0.02 kg m^{-4} vertical density gradient criteria, the pycnocline covered a wide vertical depth range of 21 – 45 m (bounded by red lines in Figures 3a and 3e) on average. Elevated velocity shear is found in the pycnocline as revealed by the shipboard ADCP measurements (Figure 3h).

Figures 3a and 3e show temporal variations of ε and χ at Stn. H08, respectively. Turbulence due to bottom friction was limited within layers deeper than 60 m, and is only visible in the first three profiles which reached closer enough to the seabed (Figure 3a). The observed bottom boundary turbulence was relatively weak due to its farness from the seabed.

The most notable feature of turbulence at Stn. H08 is that there were elevated ε (~ 10^{-7} W kg^{-1}) and χ (10^{-6} K^2 s^{-1}) in the mid column (30–40 m depth) between isopycnals of 24 kg m^{-3} and 25 kg m^{-3}. This intensified turbulence was located in the pycnocline below the depth of the strongest stratification and corresponded to a moderate stratification. It has been observed by all the eight deployed microstructure profiles spanning about 20 h.

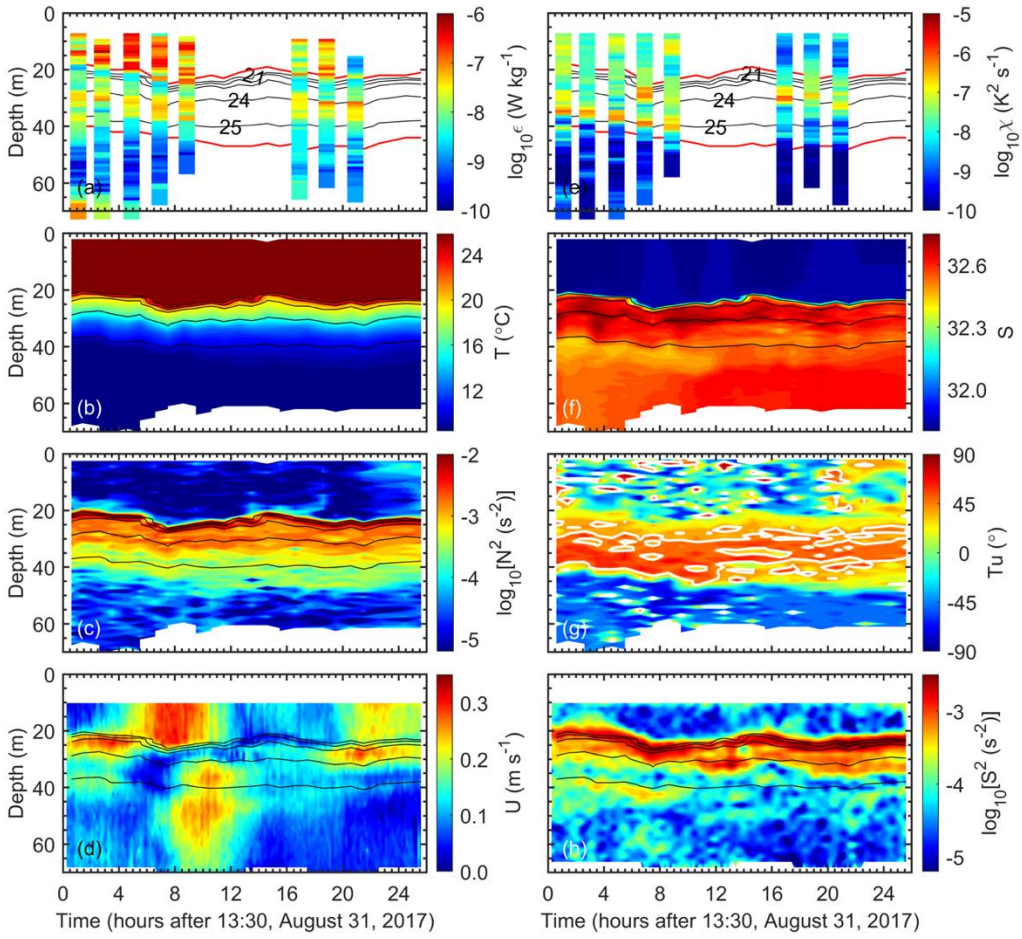

Figure 3. Time-depth variations of (a) ε, (b) temperature, (c) squared buoyancy frequency (N^2), (d) velocity magnitude, (e) χ, (f) salinity, (g) Turner angle (Tu), (h) squared shear (S^2) at Stn. H08. Black contours indicate isopycnals in 1 kg m^{-3} interval. White contours in (g) denote Tu = 45°. The red lines in (a, e) denote the upper and lower boundaries of pycnocline according to the 0.02 kg m^{-4} vertical density gradient criteria.

3.1.2 Station C05

Because of the proximity both in location and in the time of the year, Stn. C05 had similar hydrographic properties with Stn. H08. There was also a strong pycnocline separating the warm, fresh upper water and cool, salty bottom water, except that the pycnocline was shallower

than Stn. H08 (Figures 4b, 4e, and 4c). The pycnocline covered a vertical depth range of 13 – 43 m on average. The YSCWM (T < 10 °C) occupied the water column deeper than ~ 40 m.

Notably, although the measurements were carried out in different years, intensified turbulence was also observed in the pycnocline below the depth of the strongest stratification at Stn. C05 (Figures 4a and 4b). Compared to that at Stn. H08, the intensified turbulence at Stn. C05 seemed to occupy a narrower vertical range (24–30 m depth) around the isopycnals of 24 kg m^{-3}. The intensified pycnocline turbulence was also a persisting feature throughout the measurement period. In fact, Liu et al. (2009) also observed similar intensified pycnocline turbulence from their 25-hr microstructure measurements in 2006 at a station in the central YS. Strong turbulence occurred in a 6 – 7 m layer just below the strongest stratification which lasted through the observation period. This coincided well with our observations here. However, the related driving mechanism was not discussed in detail by Liu et al. (2009) due to the lack of simultaneous velocity measurements.

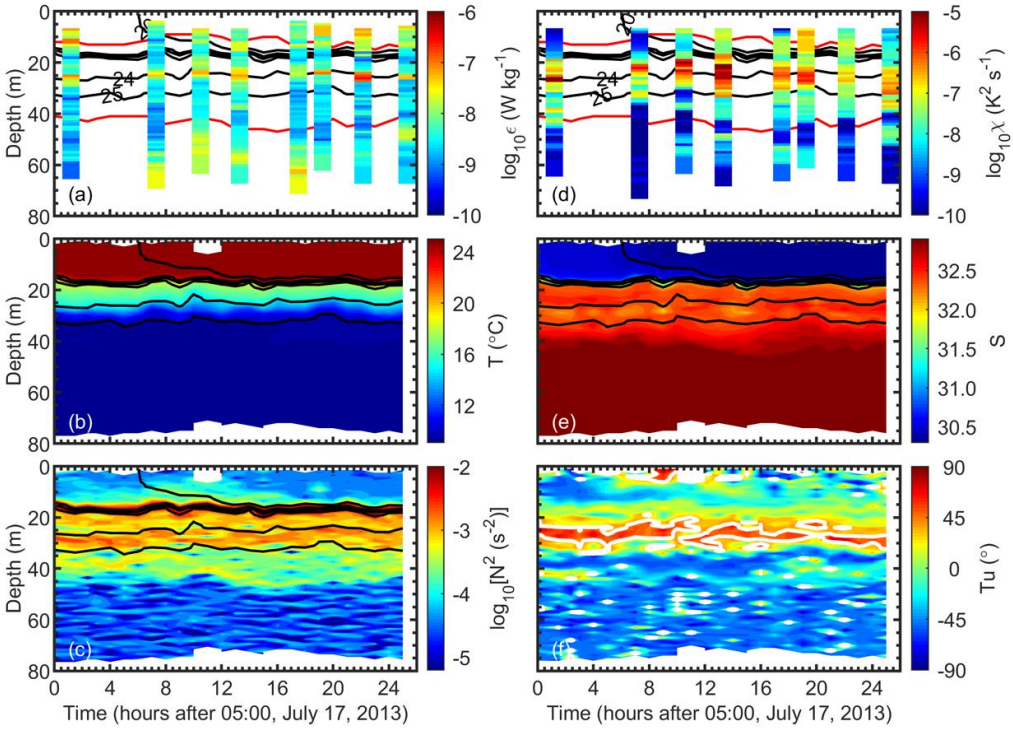

Figure 4. Time-depth variations of (a) ε, (b) temperature, (c) squared buoyancy frequency (N^2), (d) χ, (e) salinity, (f) Turner angle (Tu) at Stn. C05. Black contours in (a – e) indicate isopycnals in 1 kg m^{-3} interval. White contours in (f) denote Tu = 45°. The red lines in (a, d) denote the upper and lower boundaries of pycnocline according to the 0.02 kg m^{-4} vertical density gradient criteria.

3.2. Spatial variations of turbulence

The spatial variations of turbulence as revealed by the transect observations are next examined. The often-observed surface intensification of turbulence is not obvious because we have eliminated measurements in the upper 10 m presumably contaminated by ship-induced disturbances (Figure 5). Elevation of ε in the bottom boundary layer is evident at stations where the VMP profiles reached close enough to the seafloor. This is anticipated for the YS which is known to be a tidally energetic shelf sea (Lozovatsky et al., 2008). Most strikingly, the intensified pycnocline turbulence (ε ~ O (10^{-7} W kg^{-1}), χ ~ O (10^{-6} K^2 s^{-1})) at the two repeated sampling stations as presented above appears to be a widespread phenomenon over a large area of the YS during both cruises (Figure 5). The elevated ε was located in the pycnocline which is 1–2 orders of magnitude larger than the observed lowest ε.

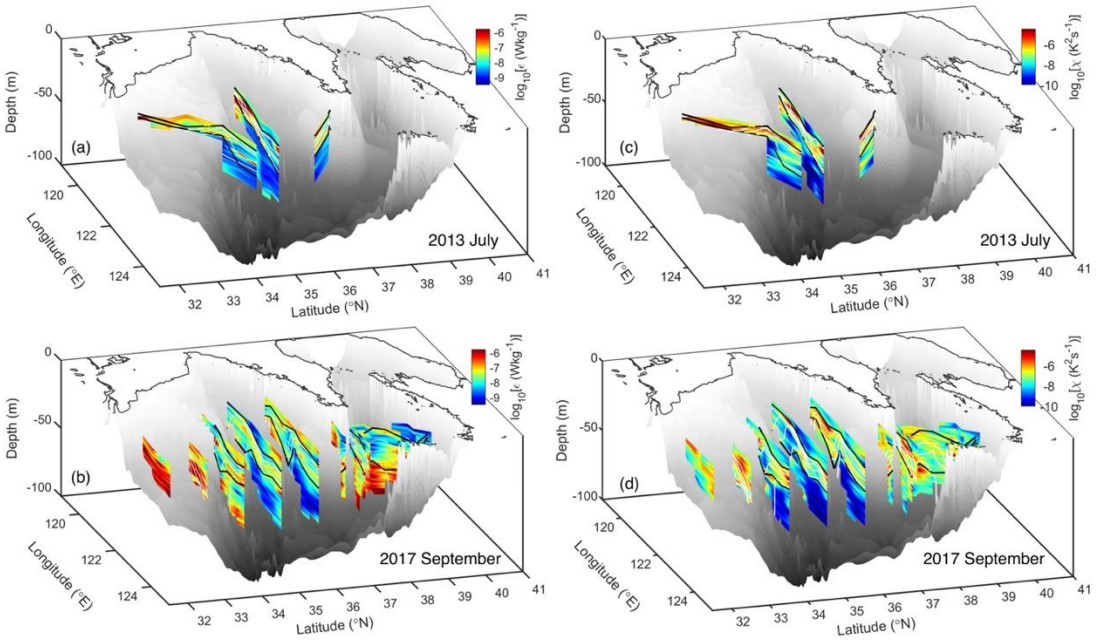

Figure 5. Spatial distributions of ε (a, b) and χ (c, d) in the YS during the two cruises: (a, c) July 2013, (b, d) September 2017. Isopycnals are overlain to indicate variations of the pycnocline. The black lines denote the upper and lower boundaries of pycnocline according to the 0.02 kg m^{-4} vertical density gradient criteria. The surface and bottom boundary layers lie above and below the pycnocline, respectively.

To reveal more clearly vertical structures of turbulence at the transect stations, we present variations of ε and χ along some representative sections. Figure 6 shows the results for sections along ~35 °N during both cruises, and along ~36 °N during the 2017 cruise. The location of the repeated sampling stations is shown by pentagrams in Figure 6d and also boxed

in Figures 6a and 6i. There are clear similar properties of intensified pycnocline turbulence between the transect and two repeated sampling stations.

Layers of elevated ε and χ occurred in the pycnocline and varied in depth following depth variations of the pycnocline (Figures 6a, b, e, f, i, j). This coincides with the results at the repeated sampling stations that intensified turbulence is located within a narrow range in isopycnals. As such, the intensified turbulence in the pycnocline has been well observed at both the transect and repeated sampling stations. The presented results are in fact similar to those of Liu et al. (2009) which revealed intensified turbulence right below the strongest stratification in a pycnocline with small vertical displacement. Just given the fact that the presented measurements here were conducted in two different years and contained both transect and repeated sampling stations, it is highly plausible to expect that the intensified pycnocline turbulence are prevailing features of the summer stratified YS.

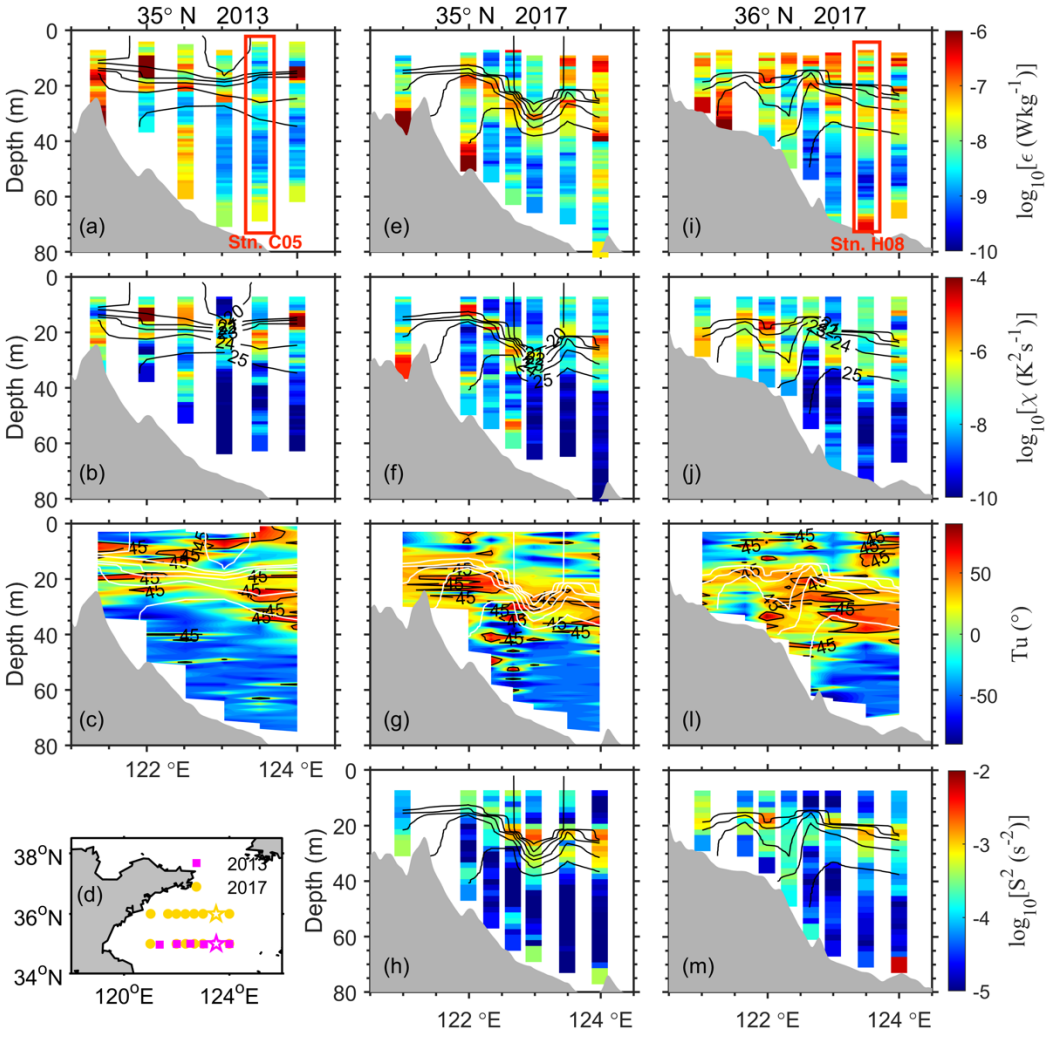

Figure 6. (a, e, i) ε, (b, f, j) χ, (c, g, l) Tu, and (h, m) squared shear at three representative transects along ~ 35°N during the 2013 (left column) and 2017 (middle column) cruises, and along ~36°N during the 2017 cruise (right column). The isopycnals are overlain. Shown in (d) are the locations of the transect stations. Pentagrams indicate the repeated sampling stations with their locations also boxed in (a) and (i).

3.3. Physical backgrounds

3.3.1 Near-inertial pycnocline shear

Physical processes that may have generated the observed intensified pycnocline turbulence in the YS are now examined. In comparison to the transect observations, the continuous sampling at a fixed location allows the examination in temporal space. We first focus on features of shear at the repeated sampling Stn. H08. Figure 3g shows that there was large velocity shear located right at the layer of the strongest stratification at Stn. H08. To address the driving mechanism of the strong velocity shear, the baroclinic velocity was next examined. Figures 7d and 7e show temporal evolutions of the zonal and meridional baroclinic velocities at Stn. H08, respectively. Both components show a dominant first-mode structure (reversed current direction above and below the pycnocline), therefore, inducing large velocity shear across the pycnocline.

Limited by the short measurement period, it is not possible to directly identify frequency content of the observed velocities through spectral analysis, but the observed surface baroclinic current at Stn. H08 (Figure 7c) seemed to have rotated clockwisely with a period (~ 21 h) approximately matching the local inertial period (20.4 h). This suggests that the baroclinic velocities may be associated with NIWs. To test this hypothesis, we conducted a quantitative analysis with the classic slab mixed-layer model. We initialized the simulation on 11 August, about 20 days before the observation period at Stn. H08, so that the model results for the periods of interest are not sensitive to the initial condition.

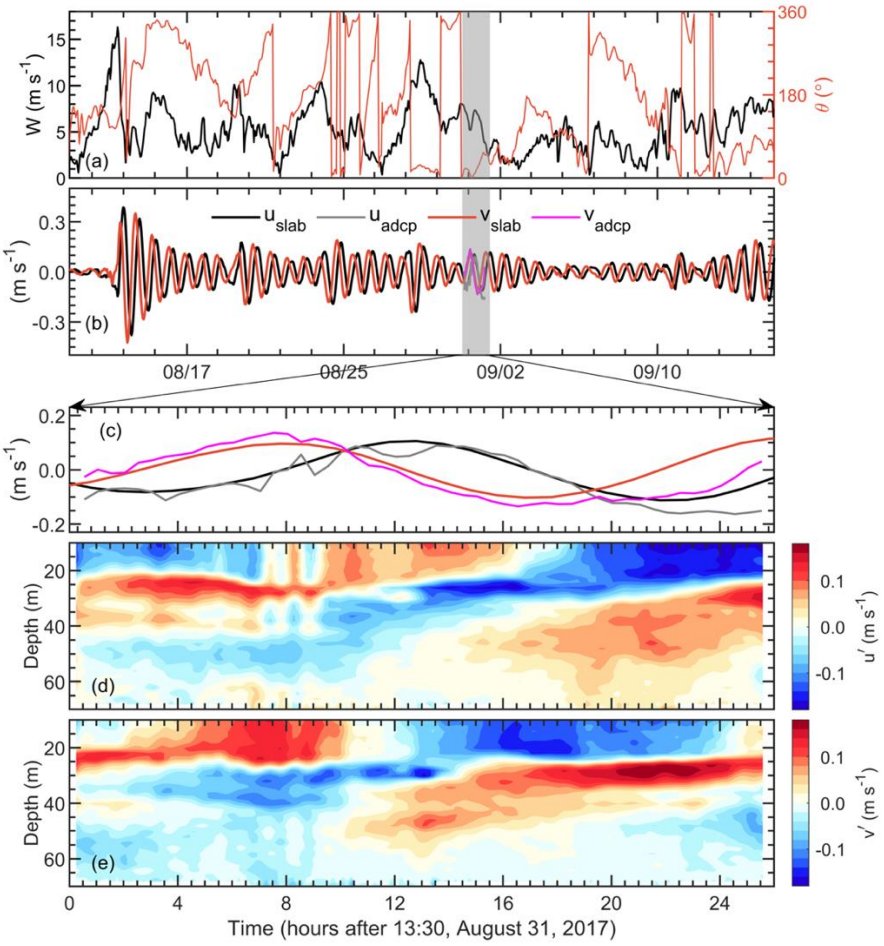

Figure 7. (a) Temporal variations of the wind speed and direction at Stn. H08. (b) Slab-model-simulated mixed layer near-inertial zonal (u_{slab}) and meridional (v_{slab}) velocities (c) Slab-model simulated mixed layer near-inertial zonal (u_{slab}) and meridional (v_{slab}) velocities compared to the surface zonal (u_{ADCP}) and meridional (v_{ADCP}) velocities observed by the shipboard ADCP. Depth-time maps of the observed (d) zonal and (e) meridional baroclinic velocities. The measurement duration is indicated by the gray shading in (a) and (b).

As shown in Figure 7b, the slab model simulated strong near-inertial responses in the mixed layer of Stn. H08. A quantitative comparison of the slab model simulations and the in-situ observations show that simulated near-inertial currents appear to agree well with the observations in phase, although there is a sizeable difference in amplitude (Figure 7c). This suggests that the baroclinic current at Stn. H08 was induced by wind-generated NIWs. We note that the internal wave fields can be quite complicated in the YS. Xu et al. (2020) observed semidiurnal internal tides at a repeated sampling station which is 108 km west of Stn. H08, but the results here show clear near-inertial response with a small pycnocline displacement. Figure 7a shows that although Stn. H08 was characterized by moderate wind speed (~ 8 m s^{-1}) during the observation period, the wind generally showed a quite intermittent feature during the one-

month period since August 13. The wind energy flux into near-inertial motions can be dominated by such intermittent events with duration of several days (Yu et al., 2022), resulting in prevailing near-inertial responses in the mixed layer (Figure 7b).

Due to the absence of simultaneous ADCP measurements during the cruise of 2013, we cannot identify the properties of shear and baroclinic velocity. In the previous work of Yang et al. (2021), based on year-long (August 2012 to July 2013) moored ADCP measurements in the southern YS, it has been demonstrated that the wind-induced NIWs can be a quite prevailing phenomenon in the YS during the warm season as a response to frequent wind pluses. Moreover, Yang et al. (2021) identified strong near-inertial responses at the mooring station (121.7°E, 35.8°N, ~180 km to Stn. C05) during the same period of the 2013 cruise in the present study (14–19 July 2013, see their Figure 9).We, therefore, anticipate that the wind-induced NIWs may be also working at our sampling stations in the 2013 cruise.

3.3.2. Low-salinity water layer

In addition to the wind-induced NIWs, we highlight the presence of an interesting phenomenon that may be related to the intensified pycnocline turbulence. We found that there existed a low-salinity water (LSW) layer at many sampling stations. The salinity inversions are compensated by the temperature so that the water is still stably stratified. The LSW layer is visible in the raw salinity profiles for both of Stns. H08 and C05 (Figures 3f and 4e). At Stn. H08, the LSW layer became thinner and weaker with time during the observation period (Figure 3f). The largest depth range and salinity anomaly (0.25) are found at the beginning of the measurements.

The upper and lower panels of Figure 8 summarize the time-averaged profiles at Stns. H08 and C05, respectively. Figures 8b and 8i show that the time-averaged LSW layer had its salinity minimum at ~ 40 m and ~ 30 m, and occupied a depth range of ~15 m and ~ 10 m for Stn. H08 and Stn. C05, respectively. The LSW produce inversions in salinity favorable for salt fingering at the upper boundary of LSW which is denoted by $Tu > 45°$ (Figures 8e and 8k). Figures 6c, 6g, and 6l show layers of $Tu > 45°$ over the representative transects which reflect the presence of LSW as those observed in the repeated sampling stations. Most of the LSW along the transect had a salinity anomaly less than 0.2 with the largest value reaching to 0.3 (not shown).

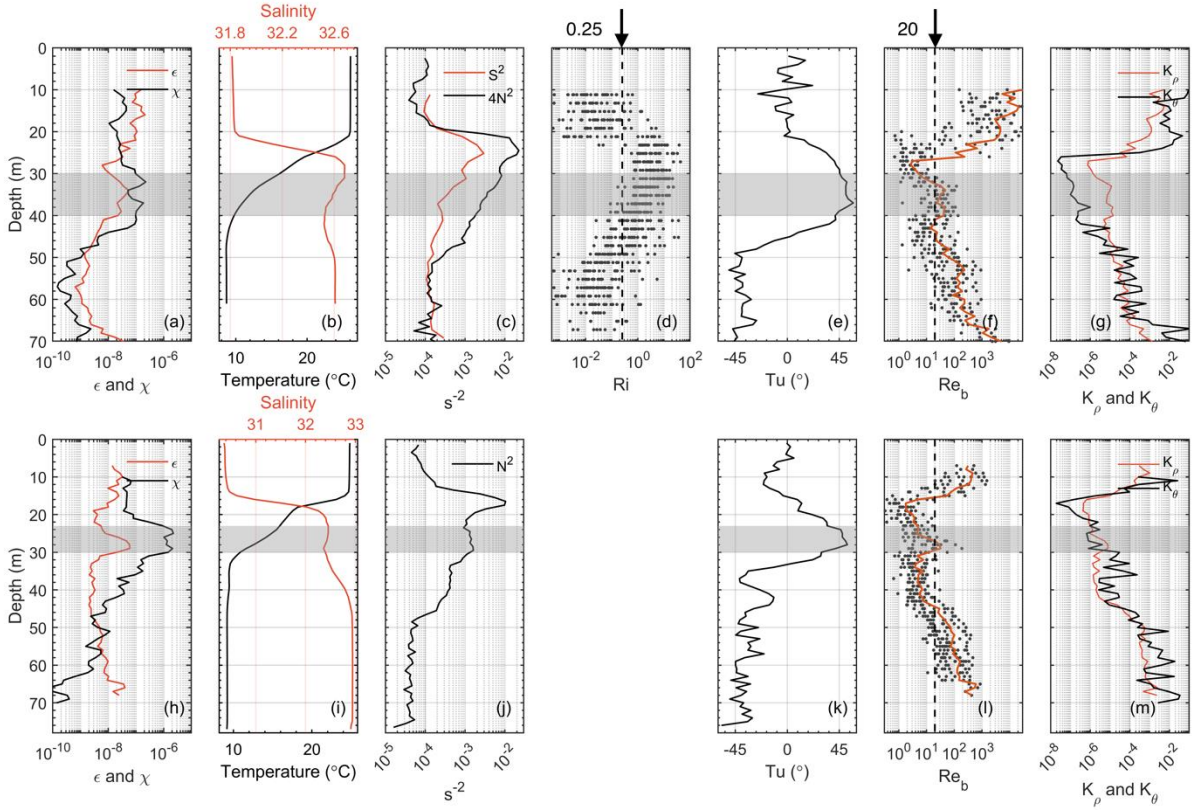

Figure 8. Time-averaged profiles at the two repeated sampling stations H08 (upper panel) and C05 (lower panel). (a, h) ε and χ, (b, i) temperature and salinity, (c, i) squared velocity shear and squared buoyancy frequency, (e, k) Turner angle, (f, l) buoyancy Reynolds number (Re_b), (g, m) K_ρ and K_θ. Also shown are the instaneous profiles of Ri at Stn. H08 (d). Gray dots in (f, l) are the instaneous profiles of Re_b. The gray shaded area in each panel indicates the identified depth ranges of intensified pycnocline turbulence (with elevated ε and χ).

To date, Zhou et al. (2004) presented the only observations of LSW in the YS using 4 CTD cruises in the period of spring and summer from June 2000 to June 2002. The LSW was suggested to be originated from the west coastal regions and intruded to the center of YS which intensifies from spring to summer. The resulting salinity inversion can reach 0.3–0.5 which is close to the value of our study. They found that the LSW had a close relationship with the tidal mixing front and suggested that the LSW was caused by the intrusion of fresher coastal water. The rare report of LSW in the YS may be due to the fact that the LSW only occupy moderate depth ranges and have in general smaller salinity differences as compared to those reported in other regions (Alford et al., 2005; Pérez-Santos et al., 2014). The features and mechanism of the LSW in the YS are interesting topics. But it is out of the scope of the present study, and we restrict our focus on the potential influence of LSW on turbulence properties at our sampling stations. The results about the spatial-temporal variability and driving mechanisms of the LSW in the southern YS will be presented in a separate study.

4. Discussion

4.1. Potential driving mechanisms of the intensified pycnocline turbulence

4.1.1. Shear instability

The most important feature as presented above is the widespread intensified turbulence below the depth of the strongest stratification in the pycnocline. There must be processes overcoming the suppressing effect of stratification on turbulence in the pycnocline. The presence of wind-induced NIWs and LSW that may be associated with the strong turbulence has been demonstrated, but how they induce the strong turbulence remain an open question.

Turbulence can be generated when the velocity shear is large enough to overcome the suppression by stable density stratification, as indicated by the Richardson number criterion for shear instabilities (Ri < 0.25; Howard, 1961; Miles, 1961; Liu, 2010). The role of velocity shear in generating the strong turbulence is first examined at Stn. H08 where we have simultaneous velocity measurements. To examine the correspondence, we plotted the profiles of S^2, N^2, Ri, and ε at Stn. H08 together (Figure 9). It is clear from Figure 9a that the observed strong turbulence was located below the strongest stratification at depths of 30–40 m. Instead, S^2 peaked right in (instead of below) the strongest stratification layer (~ 23 m depth, Figure 9b). Previous studies have also documented that the near-inertial shear was most likely quickly dissipated at the base of the mixed layer (e.g., Yu et al., 2022). There was a secondary large shear layer lying below the isopycnal of 25 kg m^{-3} at depth of ~ 40 m during the first 8 hours. However, it seems that neither of these two large shear layers coincided with the strong turbulence in depth.

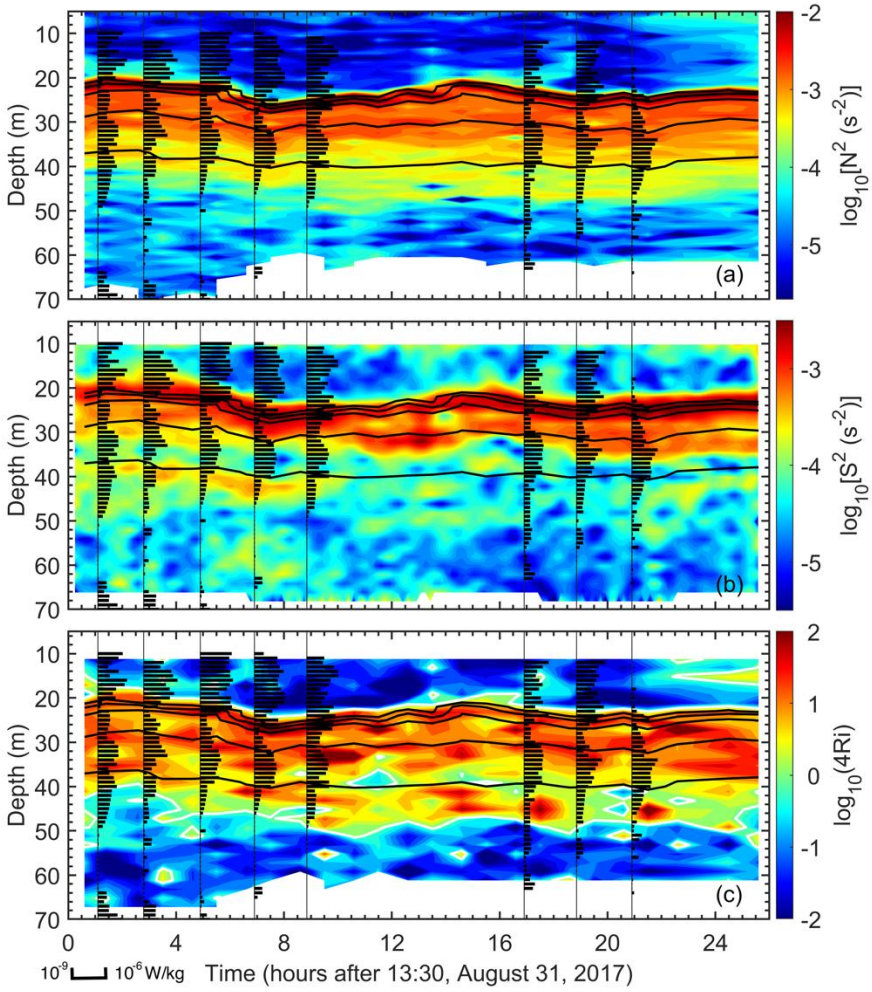

Figure 9. Time-depth variations of (a) S^2, (b) N^2, (c) Ri at Stn. H08. Black contours in all panels indicate isopycnals in 1 kg m^{-3} interval. Superimposed plots are profiles of ε. White contours in (c) indicate Ri = 0.25.

The calculated Ri showed that the shear seems not large enough to overcome the suppressing effect of strong buoyancy force on turbulence having Ri overall above 0.25 in the pycnocline (Figure 9c). The scattered plots of Ri in Figure 8d show that although it has several samples smaller than 0.25 in the gray shaded area, it is overall larger than 0.25. Previous studies have also suggested a transition value of Ri $\approx$ 1 for the breakdown of a nonlinear flow (e.g., Abarbanel et al., 1984). Some (instead of many) of the samples at depths of 30–40 m (where strong turbulence exists) satisfied the looser criterion of Ri $<$ 1 (Figure 8d). However, this cannot support the scenario that the observed strong pycnocline turbulence is directly excited by shear instabilities of the near-inertial shear. One reason is that the Ri at depths of 30–40 m is much larger than those at layers of 40–50 m; however, both ε and χ are intensified at 30–40 m instead of at 40–50 m.

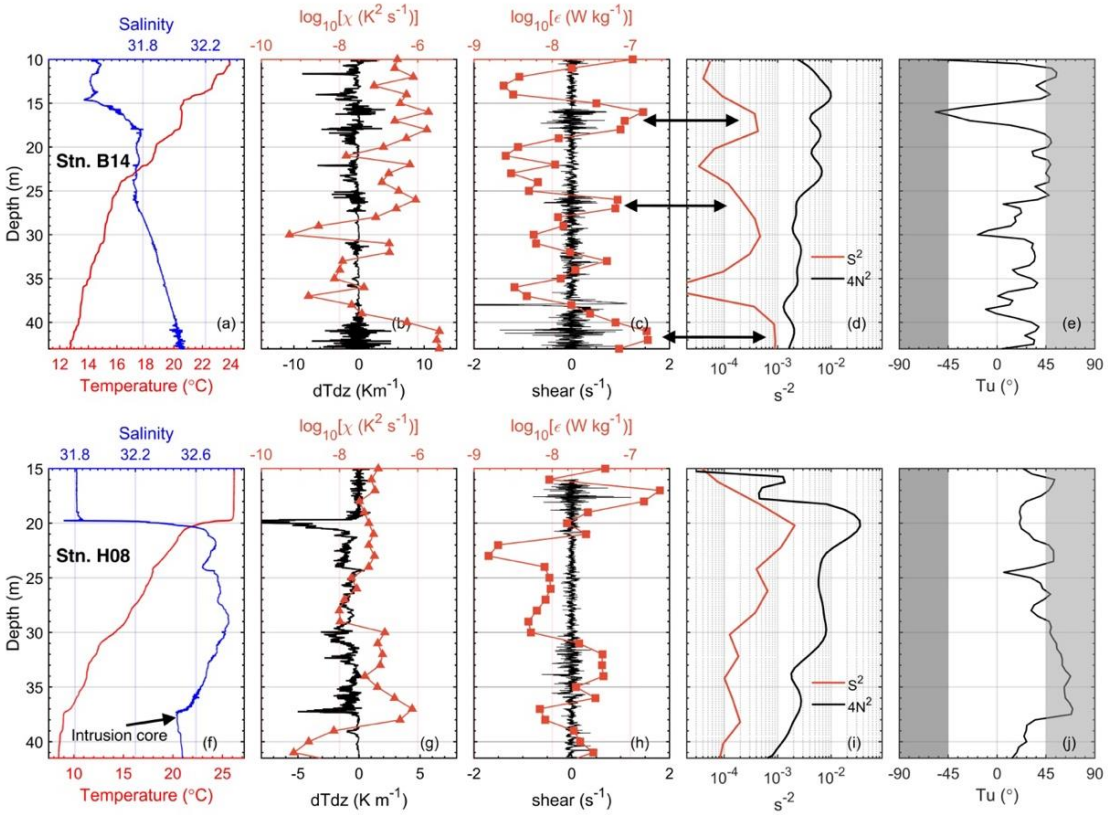

Figure 10. Vertical profiles of the observed and estimated variables at two representative stations. (a, f) temperature and salinity, (b, g) microscale temperature gradients and the estimated χ, (c, h) microscale shear and the estimated ε, (d, i) S^2 and N^2, (e, j) Tu. The upper panel shows the transect Stn. B14 (~ 122.5 °E, ~ 38 °N), and the lower panel shows the first profile (at ~ 1 h) at the repeated sampling Stn. H08. The calculation of Tu is based on 1-m averaged temperature and salinity data. The double-headed arrows in (c) and (d) emphasize the correspondence of depth between the microscale and finescale velocity shear.

One may ask: Is there any possibility that there is a vertical shift between the ADCP and CTD measurements inducing the mismatch of ε and Ri? These two instruments are carried by different platforms and the sample bins therefore may not be precisely matched, influencing the calculation of Ri. However, we suggest that this cannot be the cause of the mismatch of Ri and ε. The reason includes that there are stations show clear coincidence between enhanced velocity shear (therefore reduced Ri) and intensified turbulence.

The upper and lower panels of Figure 10 show the example VMP-measured microstructure (512 Hz) profiles at Stns. B14 and H08, respectively. Stn. B14 is located in the northern YS (~ 122.5 °E, ~ 38 °N). The microstructure profile at Stn. B14 shows three patches of strong microscale shear and thus large ε at the depth of ~16 m, ~ 27 m, and ~ 42 m (Figure

10c). Figure 10d shows that although there were no obvious layers with $S^2 > 4N^2$ (Ri < 0.25), the three observed turbulence patches were all characterized by enhanced velocity shear. The discrepancy between energetic turbulence and lack of Ri < 0.25 may be attributed to the fact that the ADCP bin size (2 m) is significantly larger than the Ozmidov scale of shear which can overestimate Ri (Moum et al., 2003). However, the coincidence in depth between enhanced velocity shear and elevated ε does suggest that the observed intensified turbulence in the pycnocline may be associated with shear instabilities of the flow.

In contrast, the depths of the shear peak and the intense microstructures were not coincident at Stn. H08 for both the example microstructure (lower panel in Figure 10) and time-averaged (upper panel in Figure 8) profiles; there was a ~ 10 m distance between the two. The linear stability analysis has also been performed at Stn. H08 via solving the Taylor-Goldstein equation (Lian et al., 2020); however, the calculated depth of critical level do not coincide with that of the observed intensified turbulence (figure not shown).

4.1.2. Salt fingering

The potential influence of LSW on the intensified pycnocline turbulence is next examined. Although externally generated mechanical turbulent events can disrupt the double-diffusive microstructure when they occur in the ocean regions occupied by fingering convection (Radko, 2013), recent studies found that the double diffusion itself can also be the main mechanism in driving turbulence (Middleton & Taylor, 2020). Middleton & Taylor (2020) showed that the double diffusion can convert background potential energy into available potential energy (APE). After that, the APE was converted into kinetic energy through the vertical turbulent buoyancy flux which was balanced by ε. In such way, the double diffusion can induce both large temperature gradient and shear microstructure. This energetic framework was verified by Middleton et al. (2021) that the predicted ε induced by double diffusion compare favorably with microstructure measurements collected in the Chukchi Sea where double diffusion occurs around a warm eddy.

Similar enhanced ε has also been observed at other regions featured with thermohaline intrusions (e.g., Larson & Gregg, 1983; Pérez-Santos et al., 2014; Fine et al., 2022) which was analogous to the observational results presented here. Based on microstructure measurements in the Beaufort Sea, Fine et al. (2022) observed elevated ε along the interleaving surface of

the intrusion. The statistical analysis considering distribution of ε as a function of Richardson number and density ratio revealed that double-diffusive convection is largely responsible for the elevated ε over the survey.

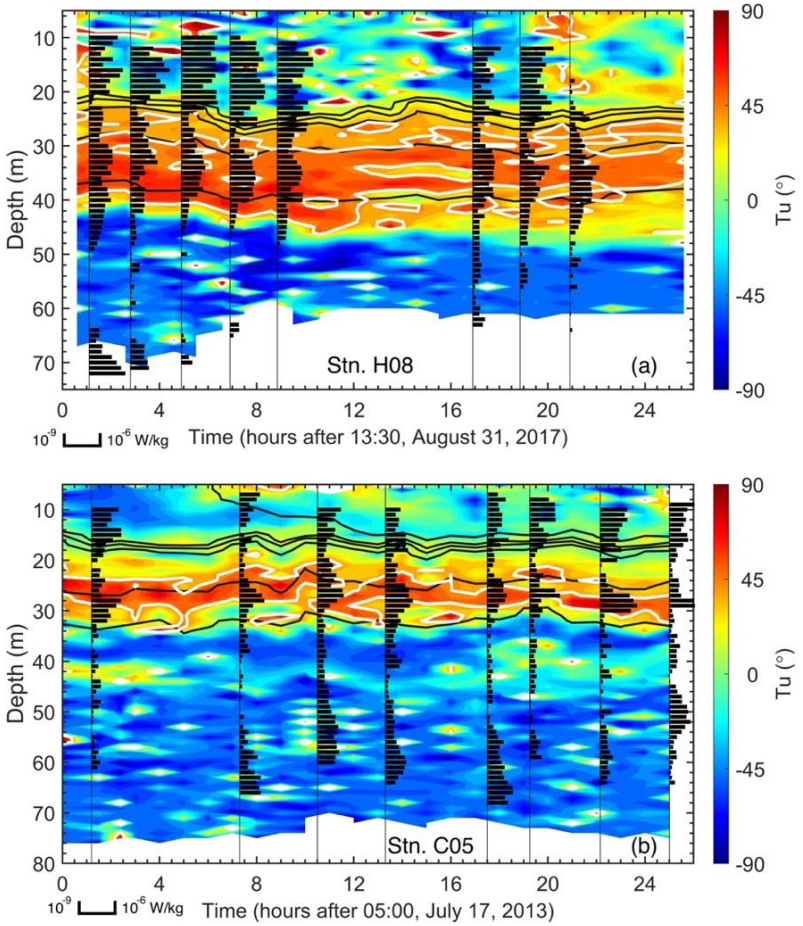

Figure 11. Time-depth variations of Tu at Stns. (a) H08 and (b) C05. Superimposed plots are profiles of ε. Black and white contours indicate isopycnals in 1 kg m^{-3} interval and Tu = 45°, respectively.

As presented above, the LSW induce inversions in salinity at the upper boundary of LSW where is favorable for salt fingering (Tu > 45°). To examine the potential role of salt fingering in generating the strong pycnocline turbulence, we replotted the profiles Tu and ε at Stns. H08 and C05 together. Figure 11 shows the time-depth variation of Tu with the profiles of ε superposed on. Both stations show persistent layers of Tu > 45° throughout the measurement period. Most importantly, layers of Tu > 45° and intensified turbulence show excellent correspondence with each other for both the occurring depth and vertical ranges. For example, the layer of Tu > 45° at Stn. H08 covers wider vertical ranges (~ 10 m) than that at Stn. C05 (~ 5 m), and so do the vertical ranges of the elevated turbulence. The time-averaged profiles of

Stns. H08 and C05 also show that the layers of Tu > 45° correspond well with the intensified turbulence (Figures 8a, e, h, k).

The example microstructure profiles at Stn. H08 show that the most intense temperature and shear microstructures were concentrated around the upper boundary of the LSW at 30 – 37 m (lower panel of Figure 10). This patch of intense microstructures is indicated by the elevated χ and ε which reached up to $\mathcal{O}$ (10^{-6} K^2 s^{-1}) and $\mathcal{O}$ (10^{-7} W kg^{-1}), respectively. Here, the upper bound of the LSW layer had Tu > 45° indicating development of salt fingers (Figure 10j), consistent with our observations of the microstructure. In contrast, there were almost no evident microstructures in the center of the LSW with χ being three orders of magnitude lower $\mathcal{O}$ (10^{-9} K^2 s^{-1}). This coincides with the recent observations in a field of intrusions south of New England which also showed virtually no and intense microstructure at and above the intrusion core, respectively (Duda et al., 2016). It is noted that for many microstructure profiles the intense microstructures were associated with temperature-compensated salinity inversions where salt fingering is expected, of which what we have just described is an example.

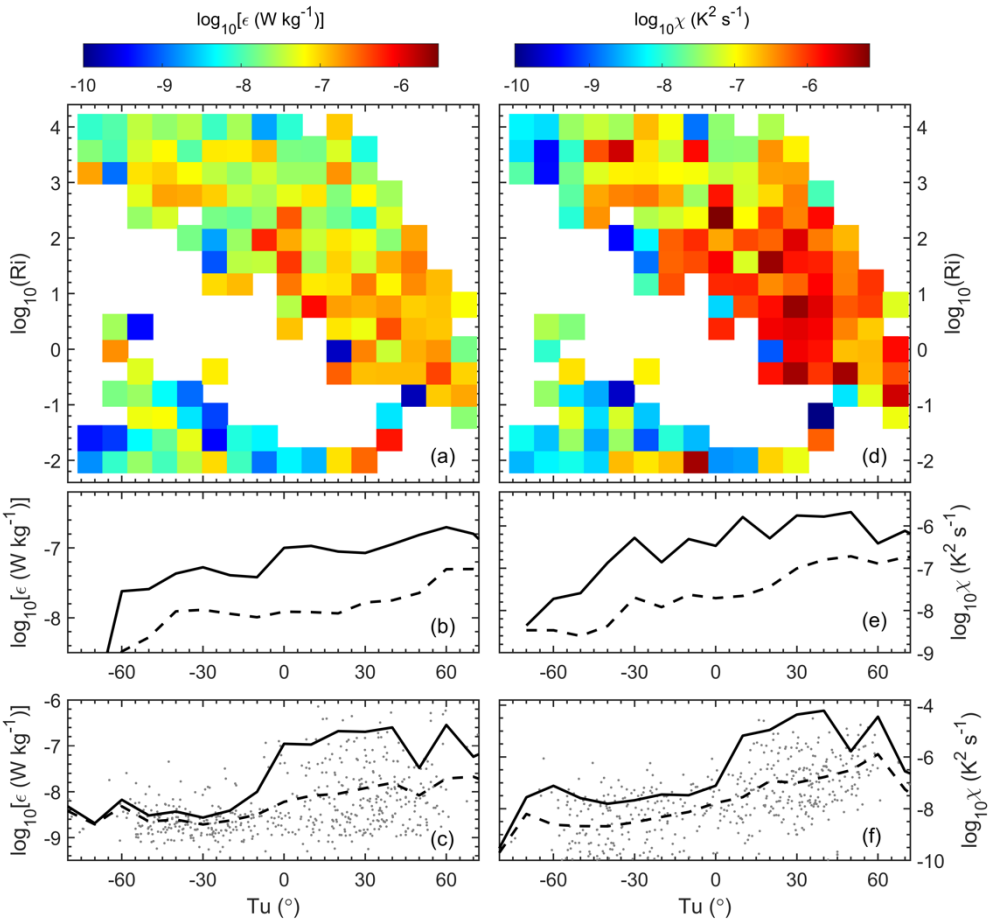

Figure 12. (a) ε and (d) χ binned in evenly spaced Turner angle (x axis) and logarithmically evenly spaced bins of Ri (y axis) based on data obtained at Stn. H08 and transect stations in

2017. Also shown are the corresponding averaged (b) ε and (e) χ as a function of Turner angle. (c) ε and (f) χ versus the Turner angle based on data obtained at Stn. C05 and transect stations in 2013. The solid and dashed lines in (b, c, e, f) denote the values bin-averaged over (ε, χ) and $log_{10}(\varepsilon, \chi)$, respectively. Note that all the comparisons are based on measurements in the stratified interior region with the surface and bottom boundary layers excluded.

To further clarify causes of the observed intensified pycnocline turbulence, we now perform a statistical correspondence analysis. Following Nagai et al. (2015), we calculated the bin-average ε and χ as a function of Tu and Ri. There are no simultaneous ADCP measurements onboard the 2013 cruise, thus ε and χ are only compared with Tu. All the comparisons are based on measurements in the pycnocline as defined by the 0.02 kg m^{-4} vertical density gradient criteria. Observations at the transect stations show a correlation trend quite similar to that at the repeated sampling stations (Stns. H08 and C05). Therefore, the results at the repeated sampling stations and transect stations are combined together. It is evident from Figure 12 that the bin-averaged ε and χ increase as the Turner angle becomes larger than 45° considering all the samples in the stratified interior region of the repeated sampling stations and transect stations. There also seem to be a very slight negative correlation between ε/χ and Ri when Tu is positive (Figures 12a and 12d). This may give some clue for the effect of shear instability; however, we note that the correlation is very weak for which the dynamics remains further study. In comparison, the correspondence with Tu is much more robust which is consistent with elevated ε and χ found in the upper interface of the LSW where salt fingering is expected.

Based on the above analysis, it is clear that intensified turbulence tends to occur at the salt-finger-favorable layer associated with the LSW; however, we caution against concluding that the observed widespread intensified pycnocline turbulence was directly generated by salt fingering. One of the reasons to this is that the previous-reported elevated ε induced by double-diffusion are at orders of $\mathcal{O}$ (10^{-8} W kg^{-1}) (Middleton et al., 2021; Fine et al., 2022), while our observed pycnocline turbulence can reach $\mathcal{O}$ (10^{-7} W kg^{-1}). The buoyancy Reynolds number ($Re_b = \varepsilon/\upsilon N^2$) was next calculated with υ the kinematic viscosity. Figures 8f and 8l show that the calculated Re_b at the intensified pycnocline turbulence layer is slightly larger than the threshold value of 20 for double-diffusion as used by Inoue et al. (2007) for Stns. H08 and C05.

To examine the driving mechanism of the observed intensified pycnocline turbulence, we next calculated the turbulent eddy diffusivity (K_ρ) following Osborn (1980) model ($K_\rho = \Gamma \frac{\varepsilon}{N^2}$, Γ =0.2) and the effective thermal diffusivity (K_θ) following Osborn and Cox (1972) model ($K_\theta = \frac{\chi}{2\overline{\theta_z}^2}$ with $\overline{\theta_z}$ the vertical temperature gradient). Larger K_θ over K_ρ is usually observed when double-diffusion plays a role in tracer vertical mixing at large (e.g., Nagai et al., 2015; George et al., 2021). Here, the calculated K_ρ and K_θ generally have close values at the boundary layers of the repeated sampling stations (Figure 8g and 8m). This is as anticipated for the shear-driven fully turbulent system. However, K_θ is smaller than K_ρ in the gray shaded layer for Stn. H08 which is in contrast to our expectation for double-diffusion regime (Figure 8m). The K_θ and K_ρ show closer values at the shaded layer for Stn. C05. The K_θ has some large values just below the shaded layer probably due to the sudden decrease of temperature gradient. However, we also do not find robust trends of $K_\theta > K_\rho$ in the shaded layer where intensified turbulence is observed.

Note that we have also examined the diffusivity results at the same three representative transects as presented in Figure 6 (Figure S1 in the supporting information). Overall, those transect stations show similar distribution with the repeated sampling stations. K_θ and K_ρ are close to each other in the boundary layers. They also have similar values across the whole water column for stations at western side of the transect where the water depth is shallow. This is as anticipated because that the bottom and surface shear-driven turbulence can influence the full water column for this shallow water. However, for the stations at eastern side of the transect where intensified pycnocline turbulence was observed, K_ρ is generally larger than K_θ in the stratified interior layer which agrees with the results at the repeated sampling stations. Besides the possible variability of Γ which might induce errors in the K_ρ calculation, we suggest that the results of large K_ρ over K_θ and the calculated Re_b again caution against concluding that the observed widespread intensified pycnocline turbulence was directly generated by salt fingering. We suggest that the driving mechanism of the intensified pycnocline turbulence may be complicated.

4.1.3. Possible complexities in the driving mechanism

Our observation is characterized by both finger-favorable stratification and background (near-inertial) shear. Recent studies showed that once there is background shear, the double-diffusive system can be quite different from the quiescent case (Smyth & Kimura, 2011, Radko, 2016). The vertical shear can be due to a variety of processes such as the NIWs. Based on linear stability analysis, Radko & Stern (2011) showed that the well-known Richardson number criterion for shear instabilities cannot be directly applied to double-diffusive fluids. The presence of background double-diffusive transports has a destabilizing effect on stratified shear flows leading to the occurrence of instabilities for Richardson numbers even exceeding unity. The mechanism is that in the presence of double diffusion, the dynamically stable shear undergoes thermohaline destabilization which produced isolated regions of reduced vertical density gradient. This, in turn, made the flow susceptible to Kelvin-Helmholtz instabilities, particularly in the zones of high background shear, resulting in intense convective mixing. The authors suggest that the results may ultimately help to explain some observations of turbulent mixing in pycnocline that is characterized by the relatively weak (Ri > 0.25) shears (Alford and Pinkel, 2000).

Recently, Tanaka et al. (2021) showed that the newly proposed instability mechanism of the onset of thermohaline-shear instability by double-diffusive convection may exists in the ocean. Based on turbulence measurement in the subarctic North Pacific, they found that the diffusive convection related inversions exhibited elevated levels of turbulence even for Ri largely exceed 0.25. This is in close agreement with our measurements suggesting the potential similar driving mechanism.

We suggest that the salt fingering associated with the LSW may cannot induce such strong turbulence in the pycnocline in the YS. Our observation resembles the numerical setting of finger-favorable stratification and background (near-inertial) shear of Radko & Stern (2011). It is hypothesized that there may exist interactions between the near-inertial velocity shear and salt fingering as discussed above, albeit how this mechanism lead to the larger K_ρ over K_θ at the intensified pycnocline turbulence layer remain unknown. Due to limitations in our observations, the exact driving mechanism of pycnocline turbulence and their role on vertical mixing awaits further investigations in the future. Regardless of the driving mechanism, our results show robust features of intensified pycnocline turbulence at the upper boundary of the LSW with excellent correspondence for both the occurring depth and vertical ranges (e.g., Figure 11). The presence of the LSW was demonstrated to play an important role in inducing pycnocline turbulence and mixing in the YS.

4.2. Implications

Tidal mixing fronts play an important role in the formation of YSCWM, which separate the cold, stratified offshore water from the warm, well-mixed shallow water near the coasts (Zhao, 1987; Lü et al., 2010; Lin et al., 2019). Previous studies have revealed the presence of an upwelling phenomenon near the front (blue arrow in Figure 13) which could be a "nutrient pump", transporting nutrients from the nutrients pool in the YSCWM to the front (Wei et al., 2018). However, the existence of the LSW as plausibly intruded from the coastal water and their potential role in biogeochemical cycles is largely ignored in previous studies (Zhou et al., 2004).

Regardless of the exact driving mechanism(s), the presence of LSW is clearly related to the layers of strong turbulence at its upper boundary (dashed arrow in Figure 13). The microstructure profiling measurements made during two summer cruises captured the same feature of intensified pycnocline turbulence which may be taken as a prevailing feature of the summer stratified YS. Apart from possible lateral intrusion of nutrients, we anticipate that the associated vertical transports as driven by the pycnocline mixing may also play a key role in supplying nutrients to the euphotic zone, having broad biogeochemical and ecological consequences (Rippeth et al., 2009; Williams et al., 2013; Yang et al., 2020).

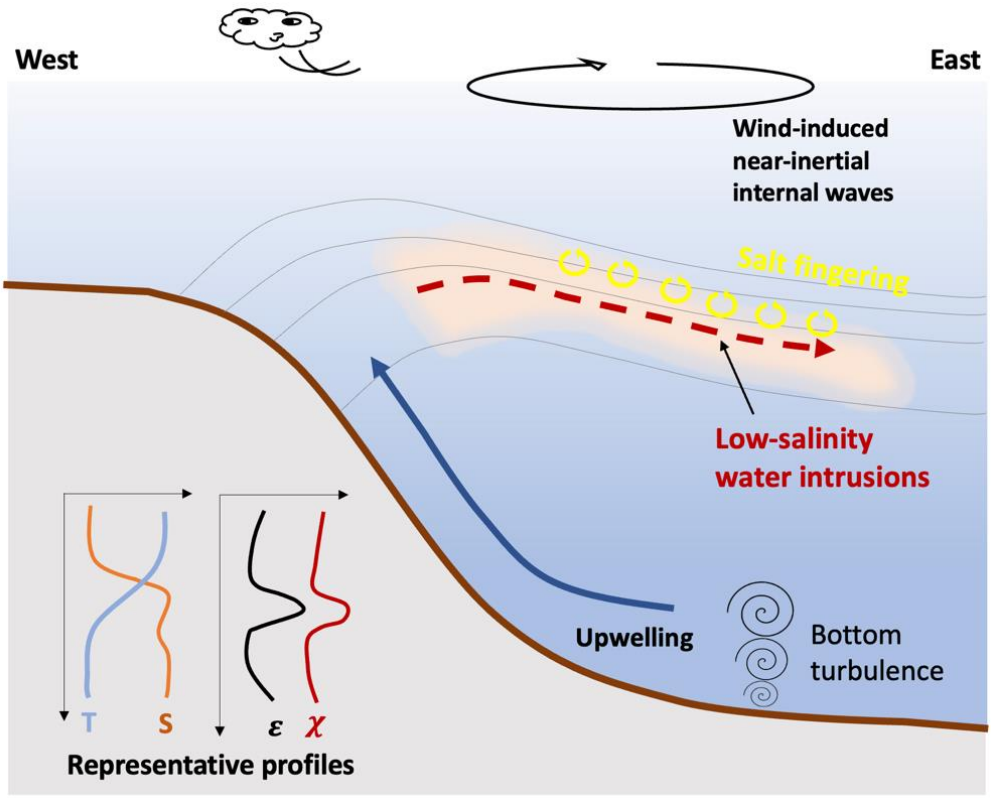

Figure 13. Schematic summary of this study. The low-salinity water which plausibly intruded from the coastal region into the central YS according to Zhou et al. (2004). This induced a salt fingering regime at its upper interface where intensified turbulence was observed. The wind disturbances generated prevailing near-inertial internal waves in the YS.

5. Concluding remarks

This study has focused on the properties of intensified pycnocline turbulence and its driving mechanisms in a typical seasonally stratified shelf sea, the Yellow Sea (YS). Based on a comprehensive dataset of microstructure measurements conducted in the summer of two years, the widespread pycnocline intensified turbulence ($\varepsilon \sim \mathcal{O}$ (10^{-7} W kg^{-1}), $\chi \sim \mathcal{O}$ (10^{-6} K^2 s^{-1})) just below the strongest stratification layer (but well above the bottom boundary layer) in the YS is revealed for the first time. This feature persisted among the two repeated sampling stations and many transect stations demonstrating its widespread nature.

Although there was evidence of wind-induced NIWs, the near-inertial shear concentrated in the pycnocline and was generally not large enough to excite shear instabilities according to the Richardson number criterion (Ri < 0.25). Instead, it is found that elevated ε and χ mostly occurred at the upper interface of a low-salinity water layer where salt fingering is expected (the Turner angle Tu > 45°). Statistical analysis shows that the bin-averaged ε and χ had a

significant correlation with Tu but not Ri. Despite the correlation with Tu, a conclusion that the intensified pycnocline turbulence was driven by salt fingering cannot be made. Our observed pycnocline turbulence can reach $\mathcal{O}$ (10^{-7} W kg^{-1}) which is one order larger than the previous-reported elevated ε induced by double-diffusion ($\mathcal{O} \sim 10^{-8}$ W kg^{-1}) (Middleton et al., 2021; Fine et al., 2022). Furthermore, the calculated Re_b is slightly larger than the threshold value of 20 for double-diffusion. We also observed larger K_ρ over K_θ at the layers with intensified pycnocline turbulence. Considering the complexities of physical environments in the study area, we further suggest the possibility of the interactions between salt fingering and near-inertial shear.

The exact mechanism(s) leading to the observed intensified pycnocline turbulence requires further studies. Nevertheless, the feature of the intensified pycnocline turbulence occurred at the upper boundary of the LSW layer is consistently revealed by the available microstructure measurements known to the authors, and is thus robust. Its widespread nature in the YS suggests its important biogeochemical and ecological implications which remain to be examined in future.

Acknowledgments.

This study was supported by the National Natural Science Foundation of China (41906006, 91858201, and 41721005). The authors are grateful to Editor Takeyoshi Nagai, and two reviewers for their valuable comments. We thank Prof. Barry R. Ruddick for providing the Maximum Likelihood Analysis codes. We thank Qiang Lian (Shantou University) for sharing the codes to solve the Taylor-Goldstein equation. The transect observations in September 2017 cruise were collected via the NSFC Open Ship-time Sharing Projects.

Data Availability Statement.

The used observational data are available at https://zenodo.org/record/6240386#.YhX1ZS2750s. The ERA5 reanalysis wind data were downloaded from https://cds.climate.copernicus.eu/cdsapp#!/home.

References

Abarbanel, H., Holm, D., Marsden, J., & Ratiu, T. (1984). Richardson number criterion for the nonlinear stability of three-dimensional stratified flow. *Physical Review Letters*, *52*, 2352-2355.

Alford, M. H., & Pinkel, R. (2000). Observations of overturning in the thermocline: The context of ocean mixing. *Journal of Physical Oceanography*, *30*, 805–832.

Alford, M. H., Gregg, M., & D'Asaro, E. (2005). Mixing, 3D Mapping, and Lagrangian evolution of a thermohaline intrusion. *Journal of Physical Oceanography*, *35*, 1689-1711.

Batchelor, G. K., (1959). Small-scale variation of convected quantities like temperature in turbulent fluid. Part 1: general discussion and the case of small conductivity. *Journal of Fluid Mechanics*, *5*(1), 113–133.

Bluteau, C. E., Lueck, R. G., Ivey, G. N., N. Jones, L. J., Book, W., & Rice, A. E. (2017). Determining mixing rates from concurrent temperature and velocity measurements. *Journal of Atmospheric and Oceanic Technology*, *34*, 2283–2293, https://doi.org/10.1175/JTECH-D-16-0250.1.

Bourgault, D., Janes, D. C., & Galbraith, P. S. (2011). Observations of a large-amplitude internal wave train and its reflection off a steep slope. *Journal of Physical Oceanography*, *41*, 586–600.

Cyr, F., Bourgault, D., & Galbraith, P. S. (2011). Interior versus boundary mixing of a cold intermediate layer, *Journal of Geophysical Research: Oceans*, *116*, C12029, doi:10.1029/2011JC007359.

D'Asaro, E. A., (1985). The energy flux from the wind to near-inertial motions in the surface mixed layer. *Journal of Physical Oceanography*, *15*(8), 1043–1059.

Duda, T. F., Lavery, A. C., & Sellers. C. J. (2016). Evaluation of an acoustic remote sensing method for frontal-zone studies using double-diffusive instability microstructure data and density interface data from intrusions. *Methods in Oceanography*, *17*, 264-281.

Fine, E. C., Mackinnon, J. A., & Alford, M. H. (2018). Microstructure observations of turbulent heat fluxes in a warm-core Canada Basin eddy. *Journal of Physical Oceanography*, *48*, 2397–2418.

Fine, E. C., Mackinnon, J. A., Alford, M. H., Middleton, L., Taylor, J., Mickett, J. B., et al (2022). Double diffusion, shear instabilities, and heat impacts of a Pacific summer water intrusion in the Beaufort Sea. *Journal of Physical Oceanography*, *52*, 189–203.

Gregg, M. C., (1999). Uncertainties and Limitations in Measuring ε and χ_T. *Journal of Atmospheric and Oceanic Technology*, *16*(11), 1483-1490. doi:10.1175/1520-0426(1999)016<1483:UALIMA>2.0.CO;2.

Gregg, M. C., & Meagher, T. B. (1980). The dynamic response of glass rod thermistors. *Journal of Geophysical Research*, *85*(C5), 2779–2786.

George, J. V., Vinayachandran, P. N., & Nayak, A. A. (2021). Enhanced double-diffusive salt flux from the high-salinity core of Arabian Sea origin waters to the Bay of Bengal. Journal of Physical Oceanography, 51, 505–518.

Howard, L.N., (1961). Note on a paper of john W. Miles. *Journal of Fluid Mechanics*, *10*(4), 509–512.

Hopkins, J., Sharples, J., & Huthnance, J. M. (2012). On-shelf transport of slope water lenses within the seasonal pycnocline. *Geophysical Research Letters*, *39*, L08604, doi:10.1029/2012GL051388.

Inoue, R., Yamazaki, H., Wolk, F., Kono, T., & Yoshida, J. (2007). An estimation of buoyancy flux for a mixture of turbulence and double diffusion. *Journal of Physical Oceanography*, *37*, 611–624.

Kimura, S., & Smyth, W. (2011). Secondary instability of salt sheets. *Journal of Marine Research*, *69*, 57-77.

Larson, N. G., & Gregg, M. C. (1983). Turbulent dissipation and shear in thermohaline intrusions. *Nature, London*, *306*, 26–32.

Liu, Z. Y., & Wei, H. (2007). Estimation of the turbulent kinetic energy dissipation rate and bottom shear stress in the tidal bottom boundary layer of the Yellow Sea. *Progress in Natural Science*, *17*(3), 289–297.

Liu, Z. Y., Wei, H., Lozovatsky, I. D., & Fernando, H. J. S., (2009). Late summer stratification, internal waves, and turbulence in the Yellow Sea. *Journal of Marine Systems*, *77*(4), 459-472. doi:10.1016/j.jmarsys.2008.11.001.

Liu. Z. Y., (2010). Instability of baroclinic tidal flow in a stratified fjord. *Journal of Physical Oceanography*, *40*, 139–154.

Liu, K., Sun, J., Guo, C., Yang, Y., Yu, W., & Wei, Z. (2019). Seasonal and spatial variations of the M2 internal tide in the Yellow Sea. *Journal of Geophysical Research: Oceans*, *124*, https://doi.org/10.1029/2018JC014819.

Li, H., & Yamazaki, H. (2001). Observations of a Kelvin-Helmholtz Billow in the Ocean. *Journal of Oceanography*, *57*, 709-721.

Lin, L., Liu, D., Luo, C., & Xie, L. (2019). Double fronts in the Yellow Sea in summertime identified using sea surface temperature data of multi-scale ultra-high resolution analysis. *Continental Shelf Research*, *175*, 76-86.

Lozovatsky, I., Liu, Z. Wei, H., & Fernando, H. J. S. (2008). Tides and mixing in the northwestern East China Sea, Part II: Near-bottom turbulence. *Continental Shelf Research*, *28*, 338-350.

Lian, Q., Smyth, W. D., & Liu, Z. (2020). Numerical computation of instabilities and internal waves from in situ measurements via the viscous Taylor-Goldstein problem. Journal of Atmospheric and Oceanic Technology. 37, 579.

MacKinnon, J. A., & Gregg, M. C. (2003). Mixing on the late-summer New England Shelf–Solibores, shear, and stratification. *Journal of Physical Oceanography*, *33*(7), 1476–1492.

Moum, J. N., Farmer, D. M., Smyth, W. D., Armi, L., & Vagle, S. (2003). Structure and generation of turbulence at interfaces strained by internal solitary waves propagating shoreward over the continental shelf. *Journal of Physical Oceanography, 33*, 2093–2112.

Middleton, L., & Taylor, J. R. (2020). A general criterion for the release of background potential energy through double diffusion. *Journal of Fluid Mechanics, 893*.

Middleton, L., Fine, E. C., MacKinnon, J. A., Alford, M. H., & Taylor, J. R. (2021). Estimating dissipation rates associated with double diffusion. *Geophysical Research Letters, 48*, e2021GL092779.

Miles, J. W., (1961). On the stability of heterogeneous shear flows. *Journal of Fluid Mechanics, 10*(4), 496–508. https://doi.org/10.1017/S0022112061000305.

Munk, W. H., & Wunsch, C., (1998). Abyssal recipes II: Energetics of tidal and wind mixing. *Deep-Sea Research I, 45*, 1977–2010. doi:10.1016/S0967-0637(98)00070-3.

Nagai, T., Durán, G. S., Otero, D. A., Mori, Y., Yoshie, N., Ohgi, K. et al. (2019). How the Kuroshio Current delivers nutrients to sunlit layers on the continental shelves with aid of

near-inertial waves and turbulence. *Geophysical Research Letters*, *46*, https://doi.org/10.1029/2019GL082680.

Nagai T., Inoue, R., Tandon, A., & Yamazaki, H. (2015). Evidence of enhanced double-diffusive convection below the main stream of the Kuroshio Extension. *Journal of Geophysical Research: Oceans*, *120*, 8402–8421. https ://doi.org/10.1007/s1023 6-003-0060-94.

Oey, L. Y., Ezer, T., Wang, D. P., Fan, S. J., & Yin, X. Q. (2006). Loop current warming by hurricane Wilma. *Geophysical Research Letters*, *33*, L08613.

Osborn, T. (1980). Estimates of the local rate of vertical diffusion from dissipation measurements, *Journal of Physical Oceanography*, 10, 83–89.

Osborn, T. R., & Cox, C. S. (1972). Oceanic fine structure, *Geophysical Fluid Dynamics*, 3, 321–345.

Palmer, M. R., Polton, J. A., Inall, M. E., Rippeth, T. P., Green, J. A. M., Sharples, J., & Simpson, J. H., (2013). Variable behavior in pycnocline mixing over shelf seas. *Geophysical Research Letters*, *40*, 161–166, doi: 10.1029/2012GL054638.

Pérez-Santos, I., Garcés-Vargas, J., Schneider, W., Parra, S., Ross, L., Valle-Levinson, A., & Parra, S., (2014). Double-diffusive layering and mixing in Patagonian fjords. *Progress in Oceanography*, *129*, 35–49.

Rayson, M., Ivey, G., Jones, N., Lowe, R., Wake, G., & McConochie, J. (2015). Near-inertial ocean response to tropical cyclone forcing on the Australian North-West Shelf. *Journal of Geophysical Research: Oceans*, *120*, 7722–7751. doi:10.1002/2015JC010868.

Radko, T. (2013). Double-diffusive convection. *Cambridge University Press*.

Radko, T., & Stern, M. (2011). Finescale instabilities of the double-diffusive shear flow. *Journal of Physical Oceanography*, *41*, 571-585.

Radko, T. (2016). Thermohaline layering in dynamically and diffusively stable shear flows. *Journal of Fluid Mechanics*, *805*, 147–170. https://doi.org/10.1017/jfm.2016.547.

Rippeth, T. P., Palmer, M. R., Simpson, J. H., Fisher, N. R., & Sharples, J. (2005). Thermocline mixing in summer stratified continental shelf sea. *Geophysical Research Letters*, *32*, L05602. doi:10.1029/2004GL022104.

Rippeth, T. P., Wiles, P., Palmer, M. R., Sharples, J., & Tweddle, J. (2009). The diapycnal nutrient flux and shear-induced diapycnal mixing in the seasonally stratified western Irish Sea. *Continental Shelf Research*, *29*, 1580–1587.

Ruddick, B. R. (1983). A practical indicator of the stability of the water column to double-diffusive activity. *Deep Sea Research*, Part A, *30*, 1105–1107.

Ruddick, B. R. (1992). Intrusive mixing in a Mediterranean salt lens: intrusion slopes and dynamical mechanisms. *Journal of Physical Oceanography*, *22*, 1274–1285.

Ruddick, B. R., Anis, A., & Thompson, K. (2000). Maximum likelihood spectral fitting: The Batchelor spectrum. *Journal of Atmospheric and Oceanic Technology*, *17*, 1541–1555.

Schmitt, R. W., (1994). Double diffusion in oceanography. *Annual Review of Fluid Mechanics*, *26*, 255–285.

Shen, J., Qiu, Y., Zhang, S., & Kuang, F. (2017). Observation of Tropical Cyclone-Induced Shallow Water Currents in Taiwan Strait. *Journal of Geophysical Research: Oceans*, *122*, 5005–5021, doi:10.1002/2017JC012737.

Simpson, J. H., & Sharples, J. (2012). Introduction to the physical and biological oceanography of shelf seas. Cambridge University Press.

Sommer, T., Carpenter, J. R., Schmid, M., Lueck, R. G., & Wuest, A. (2013). Revisiting microstructure sensor responses with implications for double-diffusive fluxes. *Journal of Atmospheric and Oceanic Technology*, *30*, 1907–1923, doi:10.1175/JTECH-D-12-00272.1.

Song, D., Gao, G., Xia, Y., Ren, Z., Liu, J., Bao, X., & Yin, B. (2021). Near-inertial oscillations in seasonal highly stratified shallow water, *Estuarine Coastal & Shelf Science, 258*, 107445, https://doi.org/10.1016/j.ecss.2021.107445.

Smyth, W., & Kimura, S. (2011). Mixing in a moderately sheared, salt fingering layer. *Journal of Physical Oceanography*, *41*, 1364–1384.

Sharples, J., & Tett, T. (1994). Modelling the effect of physical variability on the midwater chlorophyll maximum. Journal of Marine Research. 52, 219-238.

St. Laurent, L. S., & Schmitt, R. W. (1999). The contribution of salt fingers to vertical mixing in the north Atlantic tracer release experiment. *Journal of Physical Oceanography*, *29*, 1404-1424.

Tanaka, M., Yoshida, J., Lee, K., Goto, Y., Tanaka, T., Ueno, H., Onishi, H., & Yasuda, I. (2021). The potential role of thermohaline-shear instability in turbulence production in the Bering Sea and the subarctic North Pacific. *Journal of Oceanography*, *77*, 431–446. https://doi.org/10.1007/s10872-021-00602-9.

van der Lee, E. M., & Umlauf, L. (2011). Internal wave mixing in the Baltic Sea: Near-inertial waves in the absence of tides. *Journal of Geophysical Research*, *116*, C10016. doi:10.1029/2011JC007072.

Umlauf, L., Holtermann, P. L., Gillner, C. A., Prien, R. D., Merckelbach, L., & Carpenter, J. R., (2018). Diffusive convection under rapidly varying conditions. *Journal of Physical Oceanography*, *48*, 1731–1747. doi:10.1175/JPO-D-18-0018.1.

Wei, C. J., Yu, F., Guo, J. S., & Diao, X. Y., (2014). Seasonal variation of ocean turbulence in the western Yellow Sea. *Oceanol. Limnol. Sin.*, *45*(1), 166-171. (in Chinese with English abstract).

Wei, Q. S., Wang, B. D., Yao, Q. Z., Fu, M. Z., Sun, J. C., Xu, B. C., & Yu, Z. G. (2018). Hydro-biogeochemical processes and their implications for Ulva prolifera blooms and expansion in the world's largest green tide occurrence region (Yellow Sea, China). *Science of Total Environmental Sciences*, *645*, 257–266. https://doi.org/10.1016/j.scitotenv.2018.07.067.

Wolk, F., Yamazaki, H., Seuront, L., & Lueck, R. G. (2002). A New Free-Fall Profiler for Measuring Biophysical Microstructure. *Journal of Atmospheric and Oceanic Technology*, 19(5), 780-793. doi:10.1175/1520-0426(2002)019<0780:ANFFPF>2.0.CO;2.

Williams, C., Sharples, J., Mahaffey, C., & Rippeth, T. (2013). Wind-driven nutrient pulses to the subsurface chlorophyll maximum in seasonally stratified shelf seas. *Geophysical Research Letters*, *40*, 5467–5472. doi:10.1002/2013GL058171.

Woods, J., Onken, R., & Fisher, J. (1986). Thermohaline intrusions created isopycnally at oceanic fronts are inclined to isopycnals. Nature. 322, 446-448.

Xu, P. Z., Yang, W., Zhu, B. S., Wei, H., Zhao, L., & Nie, H. T. (2020). Turbulent mixing and vertical nitrate flux induced by the semidiurnal internal tides in the southern Yellow Sea. *Continental Shelf Research*, *208*, https://doi.org/10.1016/j.csr.2020.104240.

Yang, W., Wei, H., Zhao, L., & Zhang, J. (2020). Turbulence and vertical nitrate flux adjacent to the Changjiang Estuary during fall. *Journal of Marine Systems*, *212*, https://doi.org/10.1016/j.jmarsys.2020.103427.

Yang, W., Wei, H., Liu, Z., & Li, G., (2021). Intermittent intense thermocline shear associated with wind-forced near-inertial internal waves in a summer stratified temperate shelf sea. *Journal of Geophysical Research: Oceans*, *126*, e2021JC017576. https://doi.org/10.1029/2021JC017576.

Yu, X., Naveira Garabato, A. C., Vic, C., Gula, J., Savage, A. C., Wang, J., Waterhouse, A. F., & Mackinnon, J. A., (2022). Observed equatorward propagation and chimney effect of near-inertial waves in the mid-latitude ocean. *Geophysical Research Letters*, *49(13)*, e2022GL098522.

Zhao, B., (1987). A preliminary study of continental shelf fronts in the western part of southern Huanghai Sea and circulation structure in the front region of the Huanghai Cold Water Mass (HCWM). *Oceanol. Limnol. Sin. 18*(3), 217–226 (in Chinese with English abstract).

Zhou, F., Su, J., & Huang, D. (2004). Study on the inrusion of coastal low salinity water in the west of southern Huanghai Sea during spring and summer. *Acta Oceanologica Sinica*, *26*(5), 34-44. (in Chinese with English abstract).